Research Article

Ultrahigh-Sensitivity and Fast-Speed Solar-Blind Ultraviolet Photodetector Based on a Broken-Gap van der Waals Heterodiode

Li Zhang, Zhenhua Wei, Xiuxiu Wang, Luoyu Zhang, Yi Wang, Chao Xie, Tao Han, Feng Li, Wei Luo,* Dongxu Zhao, Mingsheng Long,* and Lei Shan
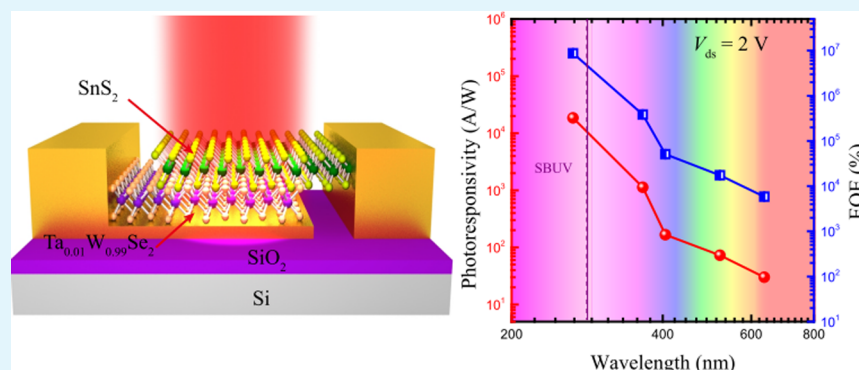
Read Online

ACCESS | Metrics & More | Article Recommendations | Supporting Information

ABSTRACT: Broad-bandgap semiconductor-based solar-blind ultraviolet (SBUV) photodetectors have attracted considerable research interest because of their broad applications in missile plume tracking, flame detectors, environmental monitoring, and optical communications due to their solar-blind nature and high sensitivity with low background radiation. Owing to its high light absorption coefficient, abundance, and wide tunable bandgap of 2−2.6 eV, tin disulfide (SnS_2) has emerged as one of the most promising compounds for application in UV−visible optoelectronic devices. However, SnS_2 UV detectors have some undesirable properties such as slow response speed, high current noise level, and low specific detectivity. This study reports a metal mirror-enhanced $Ta_{0.01}W_{0.99}Se_2/SnS_2$ (TWS) van der Waals heterodiode-based SBUV photodetector with an ultrahigh photoresponsivity (R) of ~1.85×10^4 AW^{-1} and a fast speed with rising time (τ_r) of 3.3 μs and decay time (τ_d) of 3.4 μs. Notably, the TWS heterodiode device exhibits a significantly low noise equivalent power of ~1.02×10^{-18} W Hz$^{-1/2}$ and a high specific detectivity of ~3.65×10^{14} cm Hz$^{1/2}$ W^{-1}. This study provides an alternative method for designing fast-speed SBUV photodetectors with enormous potential in applications.

KEYWORDS: photodetector, solar-blind ultraviolet, van der Waals, heterodiode, 2D materials, tin disulfide

1. INTRODUCTION

Ultraviolet photodetectors based on vdW heterojunctions by stacking dangling bonds in free two-dimensional (2D) wide-bandgap (WBG) semiconductors without being limited by the lattice matching exhibit excellent performances, such as ultrahigh photoresponsivities, ultralow dark currents, and high signal-to-noise ratios, affording them with tremendous application potential in flame tracking, missile tracking, and inter-satellite communication.[1−5] In particular, solar-blind ultraviolet (SBUV) photodetectors with low natural background noise and low probability of false alarm because of the solar irradiation wavelengths shorter than 280 nm cannot reach the earth's surface due to the strong absorption of ozone and water vapor in the atmosphere.[6,7] The high-sensitive SBUV photodetectors are highly desired for high-precision weak signal detection in this spectral range.[6,8] However, the commercially available SBUV detector (i.e., photomultiplier

tube) suffers because of its bulk structure, fragility, and large operation bias.[7,9] Various WBG semiconductors, such as AlGaN,[10] ZnMgO,[11,12] β-Ga$_2$O$_3$,[2,13−15] and diamond,[16,17] have been used in SBUV photodetectors. Self-powered model SBUV photodetectors were demonstrated based on a WBG semiconductor[18−20] without requiring a high external voltage bias. However, integration of these traditional WBG semiconductors with silicon is still challenging because of the mismatch between the lattice constants and thermal expansion coefficients of the WBG semiconductors and Si substrate.
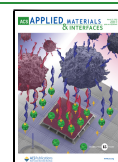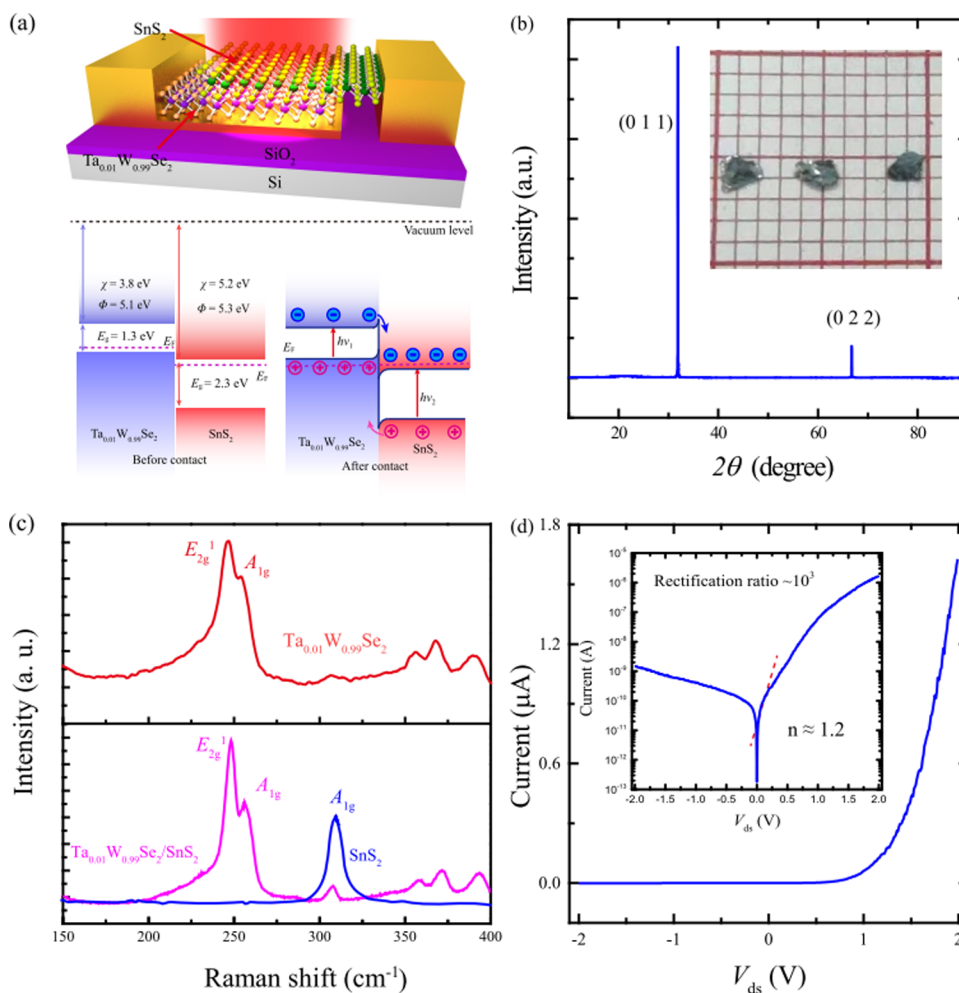
Figure 1. Structure and characterization of the TWS heterodiode device. (a) Top: schematic of the metal mirror-enhanced TWS vdW heterodiode device. Bottom: broken-gap band alignment of the TWS vdW heterostructure. (b) XRD pattern of the SnS_2 single crystal. Inset: optical photograph of the obtained SnS_2 single crystal. (c) Raman spectra of the $Ta_{0.01}W_{0.99}Se_2$, SnS_2 and TWS heterostructures. (d) $I-V$ curve of the TWS heterostructure device. Inset: semilogarithmic coordinate plot of the $I-V$ curve.

Although these WBG semiconductor-based photodetectors perform satisfactorily in their bulk forms, their performance significantly decreases on an atomic scale. A significant challenge for WBG semiconductor-based UV photodetectors is the slow response speed caused by the trap states.[21] Fortunately, dangling band-free 2D layered materials exhibit distinct advantages in the design of various heterostructures that can overcome these issues. Thus far, many 2D materials have been used as UV photodetectors, including black phosphorus,[22] bismuth oxychloride (BiOCl),[23,24] metal phosphorous tri-chalcogenides (MPX₃),[25−30] hexagonal boron nitride (h-BN),[31] 2D perovskites such as $Sr_2Nb_3O_{10}$[32] and $Cs_2AgInCl_6$,[33] and SnS_2.[34] Tin disulfide, a widely available, environmentally friendly, and chemically stable 2D layered semiconductor, has emerged as an important candidate for fabricating high-performance field-effect transistors (FETs) and low-cost, environmentally safe optoelectrical devices. SnS_2 has an indirect bandgap of 2.2−2.4 eV,[35−37] a high on/off ratio >10⁶, and a room temperature carrier mobility of up to 230 $cm^2 V^{-1} s^{-1}$ based on a solution gate.[38] High-performance UV photodetectors based on SnS_2 (~1100 AW^{-1}),[34] graphene/SnS_2 ($\sim6.35 \times 10^5$ AW^{-1}),[39] SnS_2/Si,[40] SnS_2/MoS₂,[41] and SnS_2/quantum dots mixed dimensional[42] heterostructures have been reported. However, those SnS_2-base photodetectors

demonstrated high photoresponsivity spent at the response speed, and their large dark current is also a hard nut to crack. Notably, an ultrafast photoresponse with a response time of ~5 μs was realized in a chemical vapor deposition (CVD)-grown SnS_2 phototransistor.[43] While only a low photoresponsivity of 8.8 mA W^{-1}, which may be caused by very low internal gain, has been reported based on this CVD SnS_2 phototransistor. The trade-off between a high photoresponsivity and response speed is widely observed for 2D material-based photodetectors. Using proper band alignment, such as designing a type-III broken-gap band alignment vdW heterostructures, a high-sensitive SnS_2/WSe₂ tunneling field effect transistor has demonstrated with a $\sim10^6$ light on/off ratio.[44] The highly desired SBUV photodetectors should exhibit both high sensitivity and fast response speeds. Here, a metal mirror-enhanced vdW heterodiode device is designed using p-type tungsten diselenide (WSe₂) via Ta doping[45] stacked with n-type SnS_2. The conduction band of SnS_2 is slightly lower than the valence band of WSe₂, creating the type-III broken-gap band alignment, which can be used to decrease the dark current of the SnS_2/WSe₂ heterostructure. To achieve high light absorption and photocarrier collection efficiency, the TWS vdW heterodiode was fabricated on the metal mirror electrode. The TWS vdW heterodiode exhibits excellent

performance for SBUV detection including ultrahigh photo-responsivity of $\sim 1.85 \times 10^4$ AW^{-1}, an exceptionally low noise equivalent power (NEP) of $\sim 1.02 \times 10^{-18}$ W Hz$^{-1/2}$, an ultrahigh detectivity (D^*) of $\sim 3.65 \times 10^{14}$ cm Hz$^{1/2}$ W^{-1}, a high light on/off ratio of $\sim 10^6$, and a fast speed of $\tau_r = 3.3$ μs and $\tau_d = 3.4$ μs.

2. EXPERIMENTAL SECTION

2.1. Material Synthesis. SnS$_2$ single crystals were synthesized using the self-flux method. Sn and S powders with a high purity of 99.99% were mixed in an Sn:S atomic ratio of 1:2.1. The mixture was fully ground in an agate mortar and then sealed in an evacuated ($<5 \times 10^{-4}$ Pa) quartz tube. The reagent in the quartz tube was placed in a box furnace, heated to 680 °C for 2 h, and held at 680 °C for 5 h. Then, the furnace was slowly cooled to 600 °C at a speed of 1 °C/h, subsequently switched off, and naturally cooled to room temperature. A lustrous SnS$_2$ single crystal several millimeters in size was obtained.

2.2. Ta$_{0.01}$W$_{0.99}$Se$_2$/SnS$_2$ vdW Heterodiode Device Fabrication. The TWS vdW heterostructure devices were fabricated via the dry transfer process. The prefabricated electrodes were deposited on n-type phosphor-doped silicon (0.5 mm, orient: <100>, resistivity: 0.01−0.05 Ω cm) covered by 300 nm thickness SiO$_2$. Multilayer Ta$_{0.01}$W$_{0.99}$Se$_2$ and SnS$_2$ flakes were exfoliated on polydimethylsiloxane. Then, the flakes were transferred in a sequence of first Ta$_{0.01}$W$_{0.99}$Se$_2$ and then SnS$_2$ flakes onto prefabricated Ti/Au (5/25 nm in thickness, respectively) electrodes that were treated with oxygen plasma using a home-built plasma cleaning machine before the transfer process to realize good contact between Ta$_{0.01}$W$_{0.99}$Se$_2$ and the metal electrode. Finally, the top metal electrodes were patterned via electron beam lithography. Moreover, a Cr/Au (5/40 nm in thickness, respectively) film was deposited on the patterned substrate via a thermal evaporation process.

2.3. Electrical Characterization. Electrical and photoelectrical characterizations of the fabricated Ta$_{0.01}$W$_{0.99}$Se$_2$-SnS$_2$ devices were performed using a double-channel digital source meter (Keithley 2636B). Photoresponse measurements of the Ta$_{0.01}$W$_{0.99}$Se$_2$-SnS$_2$ heterodiode in the UV spectral range were performed using unfocused light-emitting diodes (LEDs; 265 nm Thorlabs M265L5, and 365 nm Thorlabs M365L3) as light sources. Photoresponse measurements of the heterodiode in the visible spectral range were performed using 405-, 520-, and 637-nm fiber lasers which were focused on the measured heterodiode device by a 20× objective lens. To analyze the response time of the Ta$_{0.01}$W$_{0.99}$Se$_2$-SnS$_2$ vdW heterodiode, the 405-nm laser was electrically modulated by a laser diode and thermo-electric cooler controller (Thorlabs ITC4001), and a digital storage oscilloscope (Keysight, DSOX3012T Infiniium Vision) equipped with a current amplifier (SR570) was used to record the time-dependent photocurrent signal. The current noise density spectra of the heterodiode were measured using a homemade noise spectrum analyzer (NC300). To shield the electromagnetic background noise, the heterodiode device was placed in a shielded metal box with a measured bandwidth of 100 kHz at various bias voltages in ambient air.

3. RESULTS AND DISCUSSION

First, high-quality Ta$_{0.01}$W$_{0.99}$Se$_2$ single crystals were synthesized using the chemical vapor transport method. The details of the Ta$_{0.01}$W$_{0.99}$Se$_2$ growth process are reported in our previous work,[45] and the synthesis of the SnS$_2$ process is described in Section 2.1. A metal mirror-enhanced TWS vdW heterodiode photodetector was designed using a mirror metal electrode that reflects light and decreases the lateral transport distance of the photocarrier. Au, with a large work function of ~ 5.1 eV,[46] was contacted with Ta$_{0.01}$W$_{0.99}$Se$_2$ to realize good p-type semiconductor transport behavior. The transfer curve (I_{ds}-V_g) of the Ta$_{0.01}$W$_{0.99}$Se$_2$ FET is shown in Figure S1a. The device exhibits a good p-type transport property observed with

an on/off ratio of $\sim 10^4$. The SnS$_2$ FET exhibits n-type transport behavior (Figure S1b). The highly desired heterodiode with a low dark current is realized by fabricating a TWS vdW heterojunction. A schematic of the TWS vdW heterodiode is shown in Figure 1a, the under panel. The energy band structure of the Ta$_{0.01}$W$_{0.99}$Se$_2$ and SnS$_2$ before contact and the band alignment after the formation of the TWS vdW heterostructure[47] are shown in the lower panel Figure 1a. Owing to the large work function of SnS$_2$, electrons are transferred from Ta$_{0.01}$W$_{0.99}$Se$_2$ to SnS$_2$, and holes are transferred from SnS$_2$ to Ta$_{0.01}$W$_{0.99}$Se$_2$ to facilitate a new equilibrium state. To determine the quality of SnS$_2$, an SnS$_2$ single crystal was characterized using an X-ray diffractometer, and the X-ray diffraction (XRD) pattern of the SnS$_2$ single crystal is shown in Figure 1b. The SnS$_2$ single crystal exhibits the nanoflake 2T-type hexagonal structure with the space group $P\bar{3}m1$, No. 164, (JCPDS PDF number 23-0677).[48,49] Two evident diffraction peaks in the XRD spectrum at 32.19 and 67.36° are indexed to the (011) and (022) planes of the SnS$_2$ single crystal, respectively. No other orientation peaks except $(0\ h\ h)$ ($h = 1$ and 2) are observed in the XRD spectrum, as shown in Figure 1b, indicating that the SnS$_2$ single crystals grew in the (011) direction. This is different from the results of previous works on SnS$_2$ nanoplates grown on mica substrates in the (001) z direction.[50] An optical image of the SnS$_2$ single crystal is shown in the inset of Figure 1b. The SnS$_2$ single crystal has a large size of up to ~ 1 cm. Figure 1c shows the Raman spectra of Ta$_{0.01}$W$_{0.99}$Se$_2$, SnS$_2$, and the TWS vdW heterostructure. Figure 1c (top) shows the Raman spectrum of Ta$_{0.01}$W$_{0.99}$Se$_2$ flake, which has two obvious peaks at 248 and 256 cm^{-1} corresponding to the E_{2g}^1 and A_{1g} modes of the WSe$_2$, respectively.[45,51] Figure 1c (lower panel) shows the Raman spectrum of SnS$_2$ with a distinct peak at 313 cm^{-1} assigned to the A_{1g} mode of SnS$_2$, consistent with the existing literature.[38,52] The Raman spectrum of the TWS hetero-structure exhibits the typical vibration modes of Ta$_{0.01}$W$_{0.99}$Se$_2$ and SnS$_2$, but their intensities are considerably lower than those of single Ta$_{0.01}$W$_{0.99}$Se$_2$ and SnS$_2$ flakes. The lower intensity in the vdW heterostructure may be because of the interlayer charge transfer between Ta$_{0.01}$W$_{0.99}$Se$_2$ and SnS$_2$, which decreases the rate of recombination due to the separation in space of the excited carriers. The optical image of the TWS heterostructure prepared for Raman mapping is shown in Figure S2a. The Raman mappings of the TWS heterostructure on the SiO$_2$/Si substrate are shown in Figure S2b−d, which present the Raman peak of Si (peak center = 520 cm^{-1}, peak width = 20 cm^{-1}), SnS$_2$ A_{1g} mode (peak center = 315 cm^{-1}, peak width = 25 cm^{-1}), and Ta$_{0.01}$W$_{0.99}$Se$_2$ E_{2g}^1 mode (peak center = 252 cm^{-1}, peak width = 10 cm^{-1}), respectively. Figure S3 shows the elemental mappings of Ta$_{0.01}$W$_{0.99}$Se$_2$ and SnS$_2$ nanoflakes obtained by energy-dispersive X-ray spectroscopy (EDS). The EDS spectrum of the Ta$_{0.01}$W$_{0.99}$Se$_2$ nanoflakes shows uniform distributions of Ta, W, and Se, and the EDS spectrum of the SnS$_2$ nanoflakes shows uniform distributions of Sn and S. Figure S3a shows the photoluminescence (PL) spectrum of SnS$_2$. The PL spectrum of SnS$_2$ exhibits one sharp peak at 541.3 nm, corresponding to the 2.29 eV optical bandgap of SnS$_2$.[50] Figure S3b shows the PL spectrum (peak center = 541 nm and peak width = 2 nm) of the TWS heterostructure. The light area in Figure S4b corresponds to SnS$_2$. Atomic force microscopy (AFM) was used to measure the thickness of the TWS vdW heterodiode, and the AFM image of the TWS vdW heterodiode is shown in
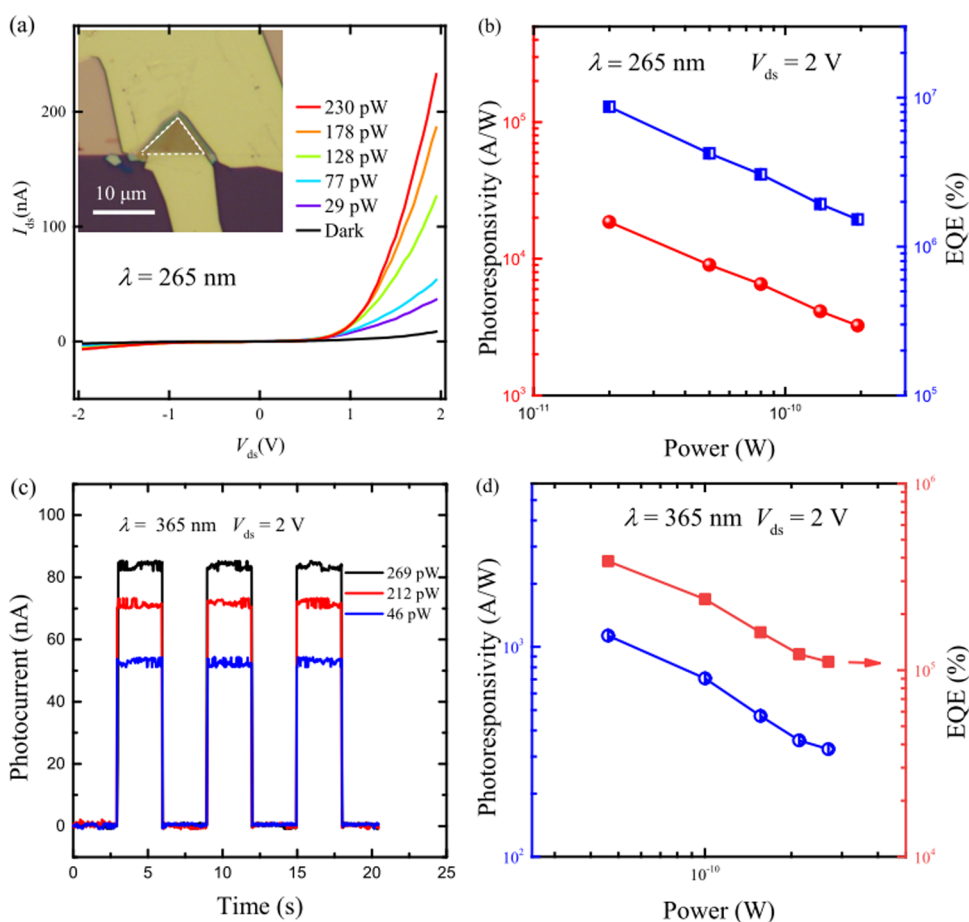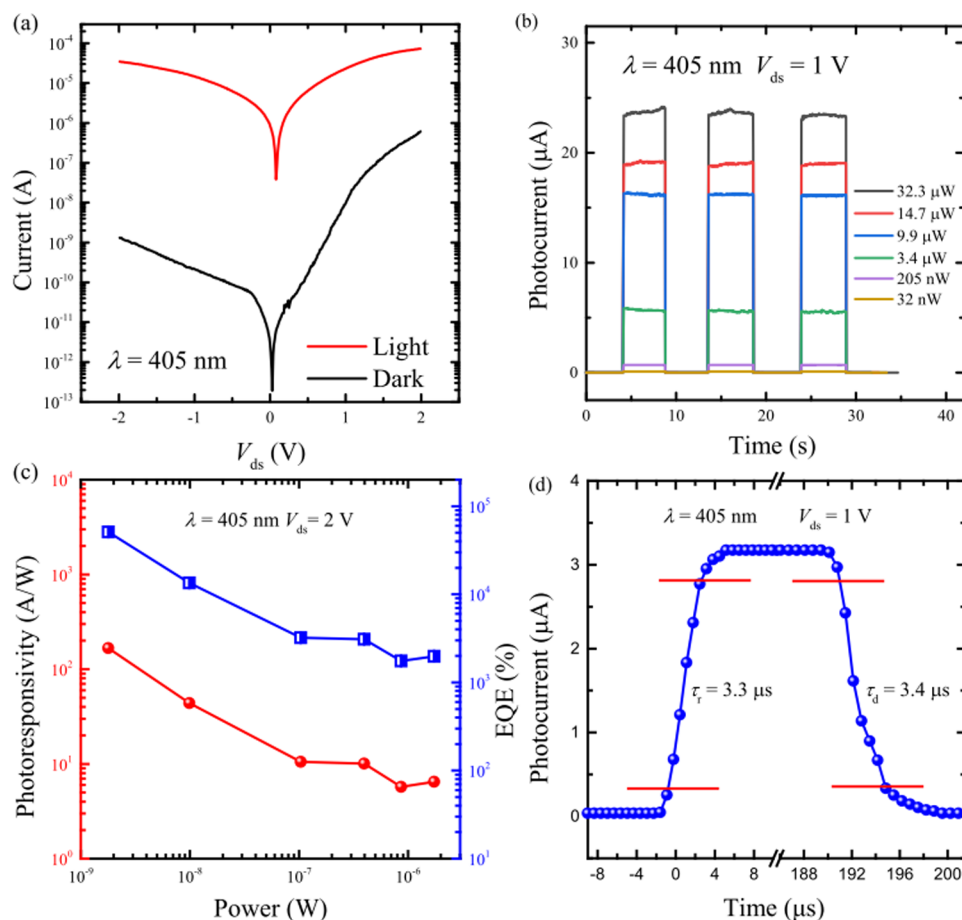
Figure 2. Photoresponse of the TWS device in the UV range. (a) $I-V$ curves of the TWS heterodiode device under various illumination powers of the 265 nm SBUV light. Inset: the optical image of the TWS heterodiode device. (b) Light power dependence of R and EQE of the TWS heterodiode device for 265 nm at V_{ds} = 2 V. (c) Time-resolved photoresponse of the device under various incidence powers of 365 nm light at V_{ds} = 2 V. (d) Extracted R and EQE of the TWS heterodiode device as functions of incident light power at V_{ds} = 2 V in ambient air.

Figure S5a. The thicknesses of $Ta_{0.01}W_{0.99}Se_2$ and SnS_2 flakes are ~42.4 and ~13.5 nm, as shown in Figure S5b,c, respectively. Next, the electronic transport behavior of the SnS_2 FET and TWS vdW junction was investigated. The $I-V$ curve of the TWS vdW heterodiode in the dark is shown in Figure 1d. The TWS vdW heterodiode device shows the rectification effect. The $I-V$ curve TWS vdW heterodiode plotted on a semilogarithmic axis is shown in the inset of Figure 1d. A high rectification ratio of ~10^3 was realized from the heterodiode, indicating the existence of the built-in electrical field. To evaluate the rectifying behavior of the TWS vdW heterodiode, the ideality factor n of the heterodiode was extracted by fitting the Shockley diode equation[53]

$$I_{ds} = I_s\left[\exp\left(\frac{qV_{ds}}{nk_BT}\right) - 1\right] \tag{1}$$

where I_s the reverse saturation current, k_B is the Boltzmann constant, and T is the temperature. An n value of 1.2, very close to 1, was extracted from the low forward bias region, indicating that the device exhibits good diode behavior. For an ideal diode, n = 1 indicates that a high-quality interface is realized with a low charge trap density. The ideality factor 20% larger than that of the ideal heterodiode confirms the high quality of the device.

Next, the photoresponse of the TWS vdW heterodiode in the UV spectral range was investigated using 265- and 365-nm LEDs. Figure 2a shows the output curves under different light powers from 29 to 230 pW and in the dark. The optical image of the TWS heterodiode device is shown in the inset of Figure 2a. The area of the TWS heterodiode device is 24.5 μm^2. At the forward bias, the currents of the TWS heterodiode considerably increased when the light was turned on. Next, the power-dependent time-resolved photoresponse of the TWS heterodiode device in the SBUV spectral range of 265 nm was measured, as shown in Figure S6a. Figure 2b shows the extracted photoresponsivity (R) and external quantum efficiency (EQE) as functions of the incident light power in the range of 20−194 pW. The photoresponsivity of the TWS heterodiode device can be obtained using the equation $R = I_P/P_I$, and it reached up to 1.85 × 10^4 AW^{-1}. The EQE can be calculated from the obtained R using the equation EQE = $hcR/(q\lambda)$ = 1240R/λ (nm). The EQE increased up to 8.68 × 10^6% at a V_{ds} = 2 V at a light power of 20 pW. The decreased tendency of R versus the light power is observed. When the light increases to 194 pW, the R and EQE decrease to 3.24 × 10^3 AW^{-1} and 1.52 × 10^6%, respectively. The rapid decrease in R in the higher power range is attributed to the limited trap states, which are saturated at a higher power density. Then, the performances of the TWS heterodiode device under illumination using a 365 nm LED were investigated. The

Figure 3. Photoresponse of the TWS vdW heterodiode. (a) Output curves of the TWS vdW heterodiode device in the presence (red) and absence (black) of illumination under a 405 nm laser. (b) Time-resolved photoresponse of the TWS heterodiode device with different illumination powers of the 405 nm laser at V_{ds} = 1 V. (c) Calculated R and EQE of the TWS heterodiode device as functions of illumination power of 405 nm laser. (d) Response speed of the TWS heterodiode under 405-nm-laser illumination at a bias of V_{ds} = 1 V.

photoresponse obtained under various fixed illumination powers by scanning the bias voltage is shown in Figure S6b. The temporal photoresponse of the heterodiode was measured at a fixed bias of 2 V, as shown in Figure 2c. The photocurrent of the TWS heterodiode device swiftly increases and decreases when the light is turned on and off, respectively. Then, the dependence of R and EQE on the light power was calculated using a 365 nm UV LED. Figure 2d shows the R and EQE as functions of the incident light power at a bias of V_{ds} = 2 V. The TWS heterodiode device exhibits an R of 1129.6 AW^{-1} and EQE of 3.83 × 10^5% under 46 pW light illumination. Decreasing tendencies of R and EQE with increasing light power are observed in Figure 2d. When the light power was increased to 269 pW, the R and EQE were 325.9 AW^{-1} and 1.11 × 10^5%, respectively. The high R was demonstrated in a large UV illumination power range, indicating that this TWS vdW heterodiode device exhibits a remarkable UV detection ability.

The photovoltaic response of the TWS vdW heterojunction was also investigated. Figure S6c shows the dependence of the photocurrent on the light power at a bias of V_{ds} = 0 V. A sublinear behavior of $I_P \propto P_I^\alpha$ with α = 0.96 < 1 was observed, and this behavior has been extensively observed for 2D material-based photodetectors because of the presence of trap centers in the channel material. The extracted photovoltaic R and EQE under 365 nm UV illumination with various powers

are shown in Figure S6d. The R and EQE showed a weak dependence on the light power at a 0 V bias and decreased from 0.176 to 0.164 AW^{-1} and 59.93 to 55.87%, respectively, when the light power was varied from 0.2 to 1.2 nW. Then, the visible light response of the metal mirror-enhanced TWS vdW heterojunction was investigated. In the visible spectral range, $Ta_{0.01}W_{0.99}Se_2$ is a major absorber of light. The TWS vdW heterodiode device performance was measured using 405, 520, and 637 nm lasers. The lasers were focused on the device with a 20× objective lens. The TWS vdW heterodiode device was placed at the center of the laser spot (∼60 μm in diameter). Figure 3a shows the I−V curves of the metal mirror-enhanced TWS vdW heterodiode devices. The measurements were performed under dark conditions at a power of 32.4 μW using a 405 nm laser. Notably, an excellent light on/off ratio of I_p/I_d over 10^6 was obtained at V_{ds} = 0 V. I−V curves of the TWS vdW heterodiode were measured by varying light powers from 32.4 nW to 32.3 μW, as shown in Figure S7a. Figure 3b shows the temporal photoresponse of a 405 nm laser at V_{ds} = 1 V with light power varying from 32 nW to 32.3 μW. The photocurrent reaches 23.5 μA with a fast response. Figure S7b shows the dependence of the photocurrent on the light power at V_{ds} = 1 V. The photocurrent exhibited a sublinear behavior with α = 0.82. Figure 3c shows the extracted R and EQE as functions of illumination power (using a 405 nm laser) at a fixed bias of V_{ds} = 2 V. The TWS vdW heterodiode exhibits an R of 166.4
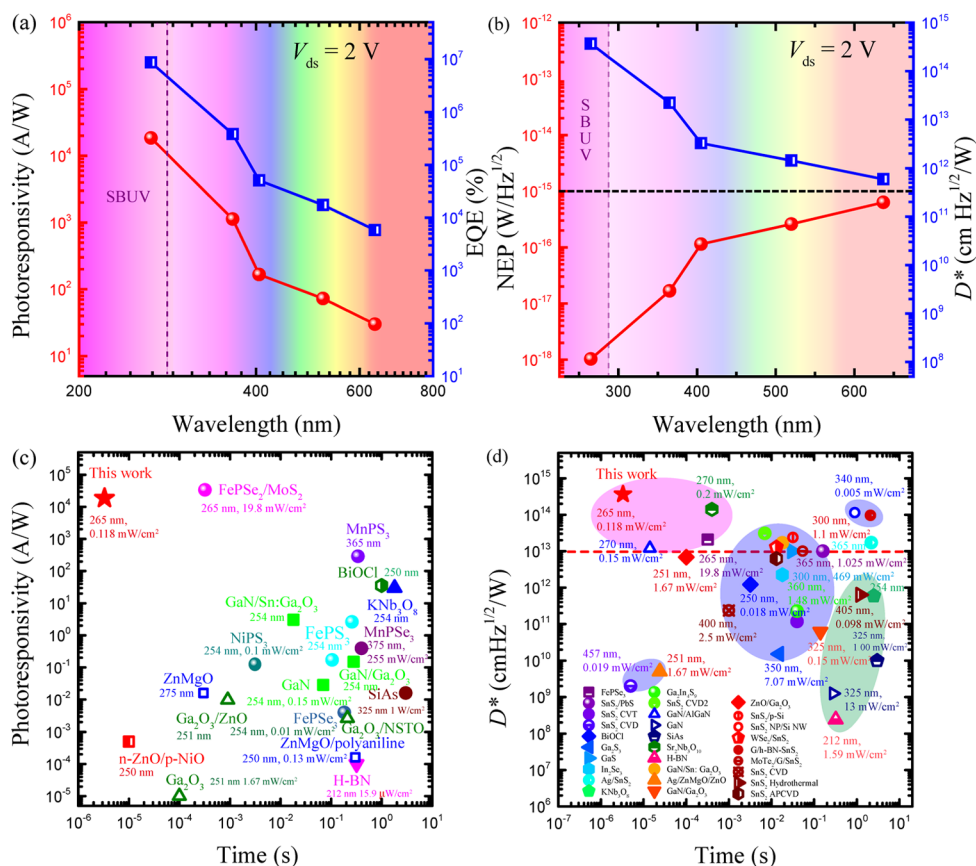
Figure 4. Comparison of the performance of the TWS vdW heterodiode. (a) R and EQE of the TWS heterodiode device as functions of incident light wavelength at $V_{ds} = 2$ V. (b) NEP and D^* of the TWS heterodiode device vs incident light wavelength at a bias of 2 V. (c) and (d) Performances of smart SBUV detectors based on 2D materials and other WBG semiconductors.

AW^{-1} and EQE of 5.09×10^4% at a power of 1.78 nW. The R and EQE in the low illumination power range ($1.7-103.9$ nW) decrease more rapidly than in the high illumination power range. In the low power range, there are adequate trap states to trap photocarriers that can obtain high photogain.[54] Then, the photoresponse of the metal mirror-enhanced TWS vdW heterodiode in the visible range ($520-637$ nm) was investigated. Figure S8a shows the output curves of the TWS vdW heterojunction devices at an illumination of 530 nW and without light. When the light is turned on, the current is considerably higher than that in the dark. The light on/off ratio of I_p/I_d was extracted over $\sim 10^4$ at a -1 V bias. Figure S8b shows the temporal photoresponse in a power range of $0.5-530$ nW of a 520 nm laser. When the laser is switched on/off, the current increases/decreases rapidly, indicating that the TWS vdW heterodiode detector has a fast photoresponse speed. A high photoresponse speed is highly desired. The speed of a device is quantified using the rising time and decay time, that is, the time of the photocurrent increasing from 10 to 90% of the maximum current when the laser is turned on and from 90 to 10% when the laser is turned off, respectively. Figure 3d shows the response time of the TWS vdW heterodiode at $V_{ds} = 1$ V measured using a 405 nm laser. The device exhibits a remarkable response speed with $\tau_r = 3.3$ μs and $\tau_d = 3.4$ μs. The TWS vdW heterodiode device exhibits both high R and good response speed, indicating that the TWS vdW heterodiode device has a high gain-bandwidth product. The realization of a high gain-bandwidth product could be attributed to a high-quality vdW heterostructure device with an

atomically sharp interface, and the mirror metal electrode enhanced vertical heterostructure device configuration, which can separate photocarrier efficiently. Figure S8c shows the sublinear light power (520 nm) dependence of the photocurrent behavior $I_P \propto P^{0.8}$. The extracted R and EQE of the TWS vdW heterodiode under 520 nm laser irradiation at a 1 V bias are shown in Figure S8d. The photoresponsivity decreases from 88.7 to 19.2 AW^{-1}, and the EQE decreases from 2.12×10^4 to 4.58×10^3% as the light power increases from 0.5 to 530 nW under 520 nm LED illumination. The photoresponse of this heterodiode device under 637 nm laser illumination was investigated. Figure S9a shows the output curves of the devices obtained in the dark and a power range from 72 to 62.3 μW of a 637 nm laser LED. The photoresponse to forward bias is significantly higher than that to the reverse bias. The time-resolved photoresponses at $V_{ds} = 1$ V were obtained by varying the light power, as shown in Figure S9b. The dependence of photocurrent on the light power exhibits sublinear behavior with a power index of $\alpha = 0.91$, as shown in Figure S9c. The parameter α obtained at the TWS vdW heterodiode device under 673 nm laser is larger than that of the TWS vdW heterodiode under 520 nm. A 520 nm laser has a higher photon energy than a 637 nm laser, and more trap states can capture photocarriers, affording a small α value. The smaller the α value, the higher the trap states that participate in current conduction.[55] Figure S9d shows the dependence of R and EQE on light power. The R and EQE of the TWS heterodiode device decrease from 19.5 AW^{-1} and 3.79×10^3% to 4.2 AW^{-1} and 827.7% as the illumination power increases from 1.48 to

1.23 μW, respectively. Furthermore, the response time was measured using a 637 nm laser with $\tau_r = 3.4$ μs and $\tau_d = 3.7$ μs, as shown in Figure S10. The high photoresponse speed is ascribed to the vertical device structure, which decreases the lateral transport distance, and the metal mirror electrode, which enhances the efficiency of photocarrier collection. Figure 4a shows the wavelength dependence of R and EQE at $V_{ds} = 2$ V. In the UV spectral range, a higher R and EQE were realized. In the visible range, the R and EQE sharply decrease from 1129.6 AW^{-1} and 3.83×10^5% to 166.3 AW^{-1} and 5.09×10^4%, respectively. The sharp decrease in R with increasing wavelength can be ascribed to the high energy trap states that considerably prolong the lifetime of the photocarrier and result in a high gain. UV spectral selectivity is an important parameter for UV detectors. The UV−visible rejection ratio (R_{265}/R_{520}) was used to evaluate the spectral selection ability of a photodetector. The high UV−visible rejection ratio of $R_{265}/R_{520} = 254.6$, a bit higher than that of $MoS_2/SnSe_2$ heterostructure (250), demonstrated based on the doped MoS_2-$SnSe_2$ heterostructure,[56] indicates that the device can operate well in the SBUV region without the influence of visible light as a background signal.

The photoresponse of the SnS_2 FET from 275 to 637 nm was also investigated for comparison. The output curves of the SnS_2 FET device were measured by the varying illumination powers of 275, 365, 405, and 637 nm lasers, as shown in Figure S11a,c,d,e, respectively. Figure S11b shows the dependence of R and EQE of the SnS_2 FET device on the power of a 275 nm laser. The SnS_2 FET device exhibits a high R of $\sim$40.8 AW^{-1} and an EQE of 1.84×10^4%. When the light power density (275 nm SBUV light) ranges from 6 to 100 mW cm^{-2}, R changes from 15.9 to 40.8 AW^{-1}, exhibiting weak light power dependence. Figure S11f exhibits the wavelength dependence of R and EQE of the SnS_2 FET at $V_{ds} = 1$ V. The R and EQE of the SnS_2 FET device decrease as the wavelength increases. Figure S12a shows the photovoltaic response of the metal mirror-enhanced TWS heterodiode. From 365 to 637 nm, the photovoltaic R of the TWS vdW heterodiode increases from 0.16 to 0.25 AW^{-1}, and the EQE decreases from 59.9 to 49.5%. Furthermore, two important properties in detectors are the NEP, which is used to quantify the sensitivity of the detector, and D^*, which determines the minimum incident light power that the detector can pick up from the background noise. To evaluate the sensitivity of this metal mirror-enhanced TWS vdW heterodiode, the current noise power spectra were measured from 1 Hz to 100 kHz at different bias voltages, and the spectra are shown in Figure S12b. When the frequency is <1 kHz, $1/f$ noise is observed that dominates the noise power contribution. The $1/f$ noise is attributed to the fluctuations of local electronic states caused by disorders or defects.[57] To calculate the NEP using the formula NEP = i_n/R, the noise current should be measured. The root-mean-square noise current $\langle i_n^2 \rangle^{1/2} = 1.02 \times 10^{-14}$ A Hz$^{-1/2}$ was obtained at an electrical bandwidth of 1 Hz at $V_{ds} = 0$ V. In the higher frequency range ($f > 1000$ Hz), the noise current density spectrum shows frequency independence and white noise behavior, which may originate from the Johnson noise or shot noise. For the shot noise, $\langle i_n^2 \rangle^{1/2} = (2eI_d)^{1/2} = 3.8 \times 10^{-16}$ A Hz$^{-1/2}$ at $I_d = 4.6 \times 10^{-13}$ A, which is significantly lower than that of the measured result. The Johnson noise $\langle i_n^2 \rangle^{1/2} = (4k_BT/R_0)^{1/2} = 1.33 \times 10^{-14}$ A Hz$^{-1/2}$ was obtained at a bandwidth of 1 Hz, $T = 300$ K, and $R_0 = 1.24$ MΩ. The Johnson noise obtained is consistent with the measured result,

indicating that Johnson noise may be the major contributor to the high-frequency noise current. D^* can be calculated using $D^* = (A\Delta f)^{1/2}/$NEP, to eliminate the influence from device area (A), and electrical bandwidth. Figure 4b shows the NEP and D^* of the heterodiode device as functions of the incident light wavelength. The black dashed line in Figure 4b marks 1 fW Hz$^{-1/2}$. The metal mirror-enhanced TWS heterodiode exhibits a significantly low NEP; a lower NEP is desirable for highly sensitive photodetectors. From SBUV to visible spectral range (265−637 nm), NEPs of our heterodiode are lower than 1 fW Hz$^{-1/2}$. Notably, the lowest NEP of 1.02×10^{-18} W Hz$^{-1/2}$ is obtained under 265 nm SBUV light. As the wavelength increases from 265 to 637 nm, the NEP of the heterodiode increases to 6.32×10^{-16} W Hz$^{-1/2}$. When the device was operated in the photovoltaic model, the NEPs from 365 to 637 nm were better than 0.1 pW Hz$^{-1/2}$, marked by a dark dashed line as shown in Figure S12c. The heterodiode device exhibits a high D^* of up to 3.65×10^{14} cm Hz$^{1/2}$ W^{-1}, realized at 265 nm SBUV light. In the UV spectral range, D^* was higher than 2.22×10^{13} cm Hz$^{1/2}$ W^{-1}. For the photovoltaic model, D^* was higher than 5.98×10^9 cm Hz$^{1/2}$ W^{-1}, as shown in Figure S12c. The performance of these smart WBG semiconductor UV photodetectors is compared and summarized in Table S1. We compared our device with state-of-the-art UV photodetectors, and the relationship between the response time and R and D^* of those UV detectors is shown in Figure 4c,d. The R of 1.85×10^4 AW^{-1} for our device is slightly lower than the record high R in the previous literature on the $FePSe_3/MoS_2$ heterodiode[29] and is considerably better than those of other listed smart UV photodetectors. The D^* of 3.65×10^{14} cm Hz$^{1/2}$ W^{-1} was one of the highest among those listed competitive UV photodetectors.

4. CONCLUSIONS

This study reports a highly sensitive SBUV photodetector based on a metal mirror-enhanced TWS vdW heterodiode. Under 265 nm SBUV light illumination, the heterodiode device exhibited a high R of 1.85×10^4 AW^{-1}, significantly low NEP of 1.02×10^{-18} W Hz$^{-1/2}$, and excellent D^* of 3.65×10^{14} cm Hz$^{1/2}$ W^{-1}. Notably, our device exhibited an ultrafast photoresponse with $\tau_r = 3.3$ μs and $\tau_d = 3.4$ μs at a 1 V bias, and high light on/off ratio of >10^6 was realized at 0 V using a 405 nm laser. The results of this study suggest that this metal mirror-enhanced TWS vdW heterodiode is a very promising SBUV photodetector with enormous potential in applications.

■ ASSOCIATED CONTENT

ⓢ Supporting Information

The Supporting Information is available free of charge at https://pubs.acs.org/doi/10.1021/acsami.2c20546.

> Transfer curves of $Ta_{0.01}W_{0.99}Se_2$ and SnS_2 field effect transistors, EDS element mapping images, PL spectrum of SnS_2, AFM image of the $Ta_{0.01}W_{0.99}Se_2$-SnS_2 heterodiode, photoresponse in the UV−visible spectral range, photoresponse time under a 637 nm laser, the photoresponse of an SnS_2 phototransistor, wavelength dependence of the NEP and D^*, current noise power density spectra of TWS vdW heterodiode with different biases, and critical parameters for 2D photodetectors (PDF)

■ AUTHOR INFORMATION

Corresponding Authors

Wei Luo − *College of Science, National University of Defense Technology, Changsha 410073, China;* ⊙ orcid.org/0000-0002-6159-9825; Email: luowei@nudt.edu.cn

Mingsheng Long − *Information Materials and Intelligent Sensing Laboratory of Anhui Province, Institutes of Physical Science and Information Technology, Anhui University, Hefei 230601, China;* ⊙ orcid.org/0000-0002-1646-7153; Email: longms@ahu.edu.cn

Authors

Li Zhang − *Information Materials and Intelligent Sensing Laboratory of Anhui Province, Institutes of Physical Science and Information Technology, Anhui University, Hefei 230601, China*

Zhenhua Wei − *College of Science, National University of Defense Technology, Changsha 410073, China*

Xiuxiu Wang − *Information Materials and Intelligent Sensing Laboratory of Anhui Province, Institutes of Physical Science and Information Technology, Anhui University, Hefei 230601, China*

Luoyu Zhang − *Information Materials and Intelligent Sensing Laboratory of Anhui Province, Institutes of Physical Science and Information Technology, Anhui University, Hefei 230601, China*

Yi Wang − *Industry-Education-Research Institute of Advanced Materials and Technology for Integrated Circuits, Anhui University, Hefei 230601, China*

Chao Xie − *Industry-Education-Research Institute of Advanced Materials and Technology for Integrated Circuits, Anhui University, Hefei 230601, China;* ⊙ orcid.org/0000-0003-4451-767X

Tao Han − *Information Materials and Intelligent Sensing Laboratory of Anhui Province, Institutes of Physical Science and Information Technology, Anhui University, Hefei 230601, China*

Feng Li − *Information Materials and Intelligent Sensing Laboratory of Anhui Province, Institutes of Physical Science and Information Technology, Anhui University, Hefei 230601, China*

Dongxu Zhao − *State Key Laboratory of Luminescence and Applications, Changchun Institute of Optics, Fine Mechanics and Physics, Chinese Academy of Sciences, Changchun 130021, China*

Lei Shan − *Information Materials and Intelligent Sensing Laboratory of Anhui Province, Institutes of Physical Science and Information Technology, Anhui University, Hefei 230601, China;* ⊙ orcid.org/0000-0001-9750-2186

Complete contact information is available at:
https://pubs.acs.org/10.1021/acsami.2c20546

Author Contributions

L.Z., Z.W., and X.W. contributed equally to this work. L.Z. carried out the experiments and wrote the draft of the manuscript. Z.W. carried out the field effect transistor device fabrication and electrical transport and Raman measurement. X.W. and L.Z. carried out device fabrication. Y.W. and C.X. helped in the solar-blind ultraviolet photoresponse measurement. T.H., F.L., L.W., D.Z., and L.S. provided experimental resources and reviewed the manuscript. M.L. designed the experiments and revised the manuscript.

Notes

The authors declare no competing financial interest.

■ REFERENCES

(1) Gorokhov, E. V.; Magunov, A. N.; Feshchenko, V. S.; Altukhov, A. A. Solar-Blind UV Flame Detector Based on Natural Diamond. *Instrum. Exp. Tech.* **2008**, *51*, 280−283.

(2) Oshima, T.; Okuno, T.; Arai, N.; Suzuki, N.; Hino, H.; Fujita, S. Flame Detection by a β-Ga$_2$O$_3$-Based Sensor. *Jpn. J. Appl. Phys.* **2009**, *48*, No. 011605.

(3) Liao, M.; Koide, Y. High-performance metal-semiconductor-metal deep-ultraviolet photodetectors based on homoepitaxial diamond thin film. *Appl. Phys. Lett.* **2006**, *89*, No. 113509.

(4) Hirano, A.; Pernot, C.; Iwaya, M.; Detchprohm, T.; Amano, H.; Akasaki, I. Demonstration of Flame Detection in Room Light Background by Solar-Blind AlGaN PIN Photodiode. *Phys. Stat. Sol. (a)* **2001**, *188*, 293−296.

(5) Pernot, C.; Hirano, A.; Iwaya, M.; Detchprohm, T.; Amano, H.; Akasaki, I. Solar-Blind UV Photodetectors Based on GaN/AlGaN p-i-n Photodiodes. *Jpn. J. Appl. Phys.* **2000**, *39*, L387−L389.

(6) Chen, Y.-C.; Lu, Y.-J.; Lin, C.-N.; Tian, Y.-Z.; Gao, C.-J.; Dong, L.; Shan, C.-X. Self-powered diamond/beta-Ga$_2$O$_3$ photodetectors for solar-blind imaging. *J. Mater. Chem. C* **2018**, *6*, 5727−5732.

(7) Guo, D.; Liu, H.; Li, P.; Wu, Z.; Wang, S.; Cui, C.; Li, C.; Tang, W. Zero-Power-Consumption Solar-Blind Photodetector Based on beta-Ga2O3/NSTO Heterojunction. *ACS Appl. Mater. Interfaces* **2017**, *9*, 1619−1628.

(8) Li, L.; Auer, E.; Liao, M.; Fang, X.; Zhai, T.; Gautam, U. K.; Lugstein, A.; Koide, Y.; Bando, Y.; Golberg, D. Deep-ultraviolet solar-blind photoconductivity of individual gallium oxide nanobelts. *Nanoscale* **2011**, *3*, 1120−1126.

(9) Li, Y.; Tokizono, T.; Liao, M.; Zhong, M.; Koide, Y.; Yamada, I.; Delaunay, J. Efficient Assembly of Bridged β-Ga2O3 Nanowires for Solar-Blind Photodetection. *Adv. Funct. Mater.* **2010**, *20*, 3972−3978.

(10) Zhang, W.; Xu, J.; Ye, W.; Li, Y.; Qi, Z.; Dai, J.; Wu, Z.; Chen, C.; Yin, J.; Li, J.; Jiang, H.; Fang, Y. High-performance AlGaN metal−semiconductor−metal solar-blind ultraviolet photodetectors by localized surface plasmon enhancement. *Appl. Phys. Lett.* **2015**, *106*, No. 021112.

(11) Fan, M.; Liu, K.; Chen, X.; Wang, X.; Zhang, Z.; Li, B.; Shen, D. Mechanism of Excellent Photoelectric Characteristics in Mixed-Phase ZnMgO Ultraviolet Photodetectors with Single Cutoff Wavelength. *ACS Appl. Mater. Interfaces* **2015**, *7*, 20600−20606.

(12) Zhao, Y.; Zhang, J.; Jiang, D.; Shan, C.; Zhang, Z.; Yao, B.; Zhao, D.; Shen, D. Ultraviolet Photodetector Based on a MgZnO Film Grown by Radio-Frequency Magnetron Sputtering. *ACS Appl. Mater. Interfaces* **2009**, *1*, 2428−2430.

(13) Zou, R.; Zhang, Z.; Liu, Q.; Hu, J.; Sang, L.; Liao, M.; Zhang, W. High Detectivity Solar-Blind High-Temperature Deep-Ultraviolet Photodetector Based on Multi-Layered (l00) Facet-Oriented β-Ga$_2$O$_3$ Nanobelts. *Small* **2014**, *10*, 1848−1856.

(14) Guo, D. Y.; Wu, Z. P.; An, Y. H.; Guo, X. C.; Chu, X. L.; Sun, C. L.; Li, L. H.; Li, P. G.; Tang, W. H. Oxygen vacancy tuned Ohmic-Schottky conversion for enhanced performance in β-Ga$_2$O$_3$ solar-blind ultraviolet photodetectors. *Appl. Phys. Lett.* **2014**, *105*, No. 023507.

(15) Suzuki, R.; Nakagomi, S.; Kokubun, Y.; Arai, N.; Ohira, S. Enhancement of responsivity in solar-blind β-Ga2O3 photodiodes with a Au Schottky contact fabricated on single crystal substrates by annealing. *Appl. Phys. Lett.* **2009**, *94*, No. 222102.

(16) Koide, Y.; Liao, M.; Alvarez, J. Thermally stable solar-blind diamond UV photodetector. *Diam. Relat. Mater.* **2006**, *15*, 1962−1966.

(17) Foulon, F.; Bergonzo, P.; Borel, C.; Marshall, R. D.; Jany, C.; Besombes, L.; Brambilla, A.; Riedel, D.; Museur, L.; Castex, M. C.; et al. Solar blind chemically vapor deposited diamond detectors for vacuum ultraviolet pulsed light-source characterization. *J. Appl. Phys.* **1998**, *84*, 5331−5336.

(18) Chen, Y.-C.; Lu, Y. L.; Lin, C.-N.; Shan, L. D. A. C. Self-powered diamond/b-Ga2O3 photodetectors for solar-blind imaging. *J. Mater. Chem. C* **2018**, *6*, 5272.

(19) Zhao, B.; Wang, F.; Chen, H.; Zheng, L.; Su, L.; Zhao, D.; Fang, X. An Ultrahigh Responsivity (9.7 mA W^{-1}) Self-Powered Solar-Blind Photodetector Based on Individual ZnO−Ga$_2$O$_3$ Heterostructures. *Adv. Funct. Mater.* **2017**, *27*, No. 1700264.

(20) Chen, H.; Yu, P.; Zhang, Z.; Teng, F.; Zheng, L.; Hu, K.; Fang, X. Ultrasensitive Self-Powered Solar-Blind Deep-Ultraviolet Photodetector Based on All-Solid-State Polyaniline/MgZnO Bilayer. *Small* **2016**, *12*, 5809−5816.

(21) Vetury, R.; Zhang, N. Q.; Keller, S.; Mishra, U. K. The impact of surface states on the DC and RF characteristics of AlGaN/GaN HFETs. *IEEE Trans. Electron Devices* **2001**, *48*, 560−566.

(22) Wu, J.; Koon, G. K. W.; Xiang, D.; Han, C.; Toh, C. T.; Kulkarni, E. S.; Verzhbitskiy, I.; Carvalho, A.; Rodin, A. S.; Koenig, S. P.; et al. Colossal Ultraviolet Photoresponsivity of Few-Layer Black Phosphorus. *ACS Nano* **2015**, *9*, 8070−8077.

(23) Han, W.; Li, C.; Yang, S.; Luo, P.; Wang, F.; Feng, X.; Liu, K.; Pei, K.; Li, Y.; Li, H.; et al. Atomically Thin Oxyhalide Solar-Blind Photodetectors. *Small* **2020**, *16*, No. 2000228.

(24) Kang, L.; Yu, X.; Zhao, X.; Ouyang, Q.; Di, J.; Xu, M.; Tian, D.; Gan, W.; Ang, C. C. I.; Ning, S.; et al. Space-confined microwave synthesis of ternary-layered BiOCl crystals with high-performance ultraviolet photodetection. *InfoMat* **2020**, *2*, 593−600.

(25) Han, X.; Song, P.; Xing, J.; Chen, Z.; Li, D.; Xu, G.; Zhao, X.; Ma, F.; Rong, D.; Shi, Y.; Islam, M. R.; Liu, K.; Huang, Y. High-Performance Phototransistors Based on MnPSe$_3$ and Its Hybrid Structures with Au Nanoparticles. *ACS Appl. Mater. Interfaces* **2021**, *13*, 2836−2844.

(26) Ramos, M.; Carrascoso, F.; Frisenda, R.; Gant, P.; Manas-Valero, S.; Esteras, D. L.; Baldov, J. J.; Coronado, E.; Castellanos-Gomez, A.; Calvo, M. R. Ultra-broad spectral photo-response in FePS$_3$ air-stable devices. *npj 2D Mater. Appl.* **2021**, *5*, 19.

(27) Gao, Y.; Lei, S.; Kang, T.; Fei, L.; Mak, C.; Yuan, J.; Zhang, M.; Li, S.; Bao, Q.; Zeng; Wang, Z.; Gu, H.; Zhang, K. Bias-switchable negative and positive photoconductivity in 2D FePS$_3$ ultraviolet photodetectors. *Nanotechnology* **2018**, *29*, No. 244001.

(28) Chu, J.; Wang, F.; Yin, L.; Lei, L.; Yan, C.; Wang, F.; Wen, Y.; Wang, Z.; Jiang, C.; Feng, L.; Xiong, J.; Li, Y.; He, J. High-Performance Ultraviolet Photodetector Based on a Few-Layered 2D NiPS$_3$ Nanosheet. *Adv. Funct. Mater.* **2017**, *27*, No. 1701342.

(29) Long, M.; Shen, Z.; Wang, R.; Dong, Q.; Liu, Z.; Hu, X.; Hou, J.; Lu, Y.; Wang, F.; Zhao, D.; Ding, F.; Tu, Y.; Han, T.; Li, F.; Zhang, Z.; Hou, X.; Wang, S.; Shan, L. Ultrasensitive Solar-blind Ultraviolet Photodetector Based on FePSe$_3$/MoS$_2$ Heterostructure Response to 10.6 μm. *Adv. Funct. Mater.* **2022**, *32*, No. 2204230.

(30) Kumar, R.; Jenjeti, R. N.; Austeria, M. P.; Sampath, S. Bulk and few-layer MnPS$_3$: a new candidate for field effect transistors and UV photodetectors. *J. Mater. Chem. C* **2019**, *7*, 324−329.

(31) Liu, H.; Meng, J.; Zhang, X.; Chen, Y.; Yin, Z.; Wang, D.; Wang, Y.; You, J.; Gao, M.; Jin, P. High-performance deep ultraviolet photodetectors based on few-layer hexagonal boron nitride. *Nanoscale* **2018**, *10*, 5559−5565.

(32) Li, S.; Zhang, Y.; Yang, W.; Liu, H.; Fang, X. 2D Perovskite Sr$_2$Nb$_3$O$_{10}$ for High-Performance UV Photodetectors. *Adv. Mater.* **2020**, *32*, No. e1905443.

(33) Luo, J.; Li, S.; Wu, H.; Zhou, Y.; Li, Y.; Liu, J.; Li, J.; Li, K.; Yi, F.; Niu, G.; Tang, J. Cs$_2$AgInCl$_6$ Double Perovskite Single Crystals: Parity Forbidden Transitions and Their Application For Sensitive and Fast UV Photodetectors. *ACS Photonics* **2018**, *5*, 398−405.

(34) Fu, Y.; Gou, G.; Wang, X.; Chen, Y.; Wan, Q.; Sun, J.; Xiao, S.; Huang, H.; Yang, J.; Dai, G. High-performance photodetectors based on CVD-grown high-quality SnS$_2$ nanosheets. *Appl. Phys. A: Mater. Sci. Process.* **2017**, *123*, 299.

(35) Zhang, X.; Meng, F.; Christianson, J. R.; Arroyo-Torres, C.; Lukowski, M. A.; Liang, D.; Schmidt, J. R.; Jin, S. Vertical Heterostructures of Layered Metal Chalcogenides by van der Waals Epitaxy. *Nano Lett.* **2014**, *14*, 3047−3054.

(36) Schlaf, R.; Lang, O.; Pettenkofer, C.; Jaegermann, W. Band lineup of layered semiconductor heterointerfaces prepared by van der Waals epitaxy: Charge transfer correction term for the electron affinity rule. *J. Appl. Phys.* **1999**, *85*, 2732−2753.

(37) Williams, R. H.; Murray, R. B.; Govan, D. W.; Thomas, J. M.; Evans, E. L. Band structure and photoemission studies of SnS$_2$ and SnSe$_2$. I. Experimental. *J. Phys. C: Solid State Phys.* **1973**, *6*, 3631.

(38) Huang, Y.; Sutter, E.; Sadowski, J. T.; Cotlet, M.; Monti, O. L. A.; Racke, D. A.; Neupane, M. R.; Wickramaratne, D.; Lake, R. K.; Parkinson, B. A.; et al. Tin Disulfide—An Emerging Layered Metal Dichalcogenide Semiconductor: Materials Properties and Device Characteristics. *ACS Nano* **2014**, *8*, 10743−10755.

(39) Cui, B.; Han, J.; Xing, Y.; Lv, W.; Lei, T.; Ma, H.; Zeng, Z.; Zhang, B. Ultrahigh Photoresponsive Photodetector Based on Graphene/SnS$_2$ van der Waals Heterostructure. *Phys. Status Solidi A* **2021**, *218*, No. 2100228.

(40) Xu, J.; Zhang, H.; Song, Z.; Xu, Y.; Peng, Q.; Xiu, X.; Li, Z.; Li, C.; Liu, M.; Man, B. SnS$_2$/Si vertical heterostructure for high-performance photodetection with large photocurrent and fast speed. *Appl. Surf. Sci.* **2020**, *506*, No. 144671.

(41) Kolli, C. S. R.; Selamneni, V.; Muñiz Martínez, B. A.; Fest Carreno, A.; Emanuel Sanchez, D.; Terrones, M.; Strupiechonski, E.; De Luna Bugallo, A.; Sahatiya, P. Broadband, Ultra-High-Responsive Monolayer MoS$_2$/SnS$_2$ Quantum-Dot-Based Mixed-Dimensional Photodetector. *ACS Appl. Mater. Interfaces* **2022**, *14*, 15415−15425.

(42) Selamneni, V.; Sahatiya, P. Mixed dimensional Transition Metal Dichalcogenides (TMDs) vdW Heterostructure based Photodetectors: A review. *Microelectron. Eng.* **2023**, *269*, No. 111926.

(43) Su, G.; Hadjiev, V. G.; Loya, P. E.; Zhang, J.; Lei, S.; Maharjan, S.; Dong, P.; Ajayan, P. M.; Lou, J.; Peng, H. Chemical Vapor Deposition of Thin Crystals of Layered Semiconductor SnS$_2$ for Fast Photodetection Application. *Nano Lett.* **2015**, *15*, 506−513.

(44) Zhou, X.; Hu, X.; Zhou, S.; Song, H.; Zhang, Q.; Pi, L.; Li, L.; Li, H.; Lü, J.; Zhai, T. Tunneling Diode Based on WSe$_2$/SnS$_2$ Heterostructure Incorporating High Detectivity and Responsivity. *Adv. Mater.* **2018**, *30*, No. 1703286.

(45) Fu, Y.; Long, M.; Gao, A.; Wang, Y.; Pan, C.; Liu, X.; Zeng, J.; Xu, K.; Zhang, L.; Liu, E.; Hu, W.; Wang, X.; Miao, F. Intrinsic p-type W-based transition metal dichalcogenide by substitutional Ta-doping. *Appl. Phys. Lett.* **2017**, *111*, No. 043502.

(46) Eastman, D. E. Photoelectric Work Functions of Transition, Rare-Earth, and Noble Metals. *Phys. Rev. B* **1970**, *2*, 1.

(47) Aretouli, K. E.; Tsoutsou, D.; Tsipas, P.; Marquez-Velasco, J.; Aminalragia Giamini, S.; Kelaidis, N.; Psycharis, V.; Dimoulas, A. Epitaxial 2D SnSe$_2$/ 2D WSe$_2$ van der Waals Heterostructures. *ACS Appl. Mater. Interfaces* **2016**, *8*, 23222−23229.

(48) Zhou, X.; Zhang, Q.; Gan, L.; Li, H.; Zhai, T. Large-Size Growth of Ultrathin SnS$_2$ Nanosheets and High Performance for Phototransistors. *Adv. Funct. Mater.* **2016**, *26*, 4405−4413.

(49) Xia, J.; Zhu, D.; Wang, L.; Huang, B.; Huang, X.; Meng, X.-M. Large-Scale Growth of Two-Dimensional SnS$_2$ Crystals Driven by

Screw Dislocations and Application to Photodetectors. *Adv. Funct. Mater.* **2015**, *25*, 4255−4261.

(50) Yang, D.; Li, B.; Hu, C.; Deng, H.; Dong, D.; Yang, X.; Qiao, K.; Yuan, S.; Song, H. Controllable Growth Orientation of SnS$_2$ Flakes for Low-Noise, High-Photoswitching Ratio, and Ultrafast Phototransistors. *Adv. Opt. Mater.* **2016**, *4*, 419−426.

(51) Del Corro, E.; Terrones, H.; Elias, A.; Fantini, C.; Feng, S.; Nguyen, M. A.; Mallouk, T. E.; Terrones, M.; Pimenta, M. A. Excited Excitonic States in 1L, 2L, 3L, and Bulk WSe$_2$ Observed by Resonant Raman Spectroscopy. *ACS Nano* **2014**, *8*, 9629−9635.

(52) Smith, A. J.; Meek, P. E.; Liang, W. Y. Raman scattering studies of SnS$_2$ and SnSe$_2$. *J. Phys. C: Solid State Phys.* **1977**, *10*, 1321−1323.

(53) Banwell, T. C.; Jayakumar, A. Exact analytical solution for current flow through diode with series resistance. *Electron. Lett.* **2000**, *36*, 291−292.

(54) Guo, Q.; Pospischil, A.; Bhuiyan, M.; Jiang, H.; Tian, H.; Farmer, D.; Deng, B.; Li, C.; Han, S.; Wang, H.; Xia, Q.; Ma, T. P.; Mueller, T.; Xia, F. Black Phosphorus Mid-Infrared Photodetectors with High Gain. *Nano Lett.* **2016**, *16*, 4648−4655.

(55) Zhao, Q.; Wang, W.; Carrascoso-Plana, F.; Jie, W.; Wang, T.; Castellanos-Gomez, A.; Frisenda, R. The role of traps in the photocurrent generation mechanism in thin InSe photodetectors. *Mater. Horiz.* **2020**, *7*, 252−262.

(56) Yu, Y.; Shen, T.; Long, H.; Zhong, M.; Xin, K.; Zhou, Z.; Wang, X.; Liu, Y. Y.; Wakabayashi, H.; Liu, L.; Yang, J.; Wei, Z.; Deng, H. X. Doping Engineering in the MoS$_2$/SnSe$_2$ Heterostructure toward High-Rejection-Ratio Solar-Blind UV Photodetection. *Adv. Mater.* **2022**, *34*, No. 2206486.

(57) Clément, N.; Nishiguchi, K.; Fujiwara, A.; Vuillaume, D. One-by-one trap activation in silicon nanowire transistors. *Nat. Commun.* **2010**, *1*, 92.

📖 Recommended by ACS